

Charge Separation Efficiency in $\text{WO}_3/\text{BiVO}_4$ Photoanodes with CoFe Prussian Blue Catalyst Studied by Wavelength-Dependent Intensity-Modulated Photocurrent Spectroscopy

Pierpaolo Vecchi, Alberto Piccioni, Raffaello Mazzaro,* Michele Mazzanti, Vito Cristino, Stefano Caramori, and Luca Pasquini*

The understanding of charge carrier dynamics in complex heterojunctions is of the utmost importance for the performance optimization of photoelectrochemical cells, especially in operando. Intensity-modulated photocurrent spectroscopy (IMPS) is a powerful tool to this aim, but the information content provided by this technique can be further enhanced by selectively probing each layer of complex heterojunctions by means of multiple excitation sources. Herein, the charge carrier dynamics of a $\text{WO}_3/\text{BiVO}_4/\text{CoFe-PB}$ heterojunction, used in a conventional three electrode cell for water splitting, is studied using wavelength-dependent IMPS (WD-IMPS). The proposed data analysis allows us to identify the occurrence of interface recombination processes affecting the semiconductor junction, as well as the positive contribution of the inorganic complex catalyst on the charge separation efficiency of the BiVO_4 layer. The deep understanding of the fate of charge carriers in the studied photoanode validates WD-IMPS as a straightforward method to widen the understanding of such structures.

1. Introduction

The conversion of sunlight into fuels represents one of the few sustainable solutions to the ever-growing demand of the energy market, currently undergoing a transition from fossil fuels to renewable energy sources. Among the different processes

P. Vecchi, A. Piccioni, R. Mazzaro, L. Pasquini
Department of Physics and Astronomy
University of Bologna
Viale Bertini Pichat 6/2, 40127 Bologna, Italy
E-mail: raffaello.mazzaro@unibo.it; luca.pasquini@unibo.it

A. Piccioni, R. Mazzaro, L. Pasquini
Institute for Microelectronics and Microsystems
National Research Council
via Gobetti 101, 40129 Bologna, Italy

M. Mazzanti, V. Cristino, S. Caramori
Department of Chemical and Pharmaceutical Sciences
University of Ferrara
Via Fossato di Mortara 17, 44121 Ferrara, Italy

 The ORCID identification number(s) for the author(s) of this article can be found under <https://doi.org/10.1002/solr.202200108>.

© 2022 The Authors. Solar RRL published by Wiley-VCH GmbH. This is an open access article under the terms of the Creative Commons Attribution License, which permits use, distribution and reproduction in any medium, provided the original work is properly cited.

DOI: 10.1002/solr.202200108

yielding chemical fuels using solar energy, the photoelectrochemical (PEC) splitting of water into molecular hydrogen and oxygen has a leading role, enabling the storage of intermittent renewable solar energy^[1] through clean, waste-free chemistry. Metal oxide semiconductors (MOS) are promising materials to be used in PEC devices because of their good stability, cost-effectiveness, nontoxicity, and light-harvesting properties over the visible spectrum.^[2] Due to their deep valence band and the resistance against photocorrosion in oxidative environment, MOS are often used as photoanodes in a tandem PEC configuration to drive the oxygen evolution reaction (OER) in a separated environment.

These materials need to efficiently absorb light, have good bulk transport properties to separate the photogenerated charges, and induce fast charge transfer from the electrode inside the solution to promote the OER, often with the help of surface catalysts.^[3–5]

Heterojunctions based on $\text{WO}_3/\text{BiVO}_4$ semiconductors currently represent the state of the art in terms of photoanodes for OER.^[6,7] WO_3 is an MOS providing excellent electron mobility and good chemical stability in acidic aqueous solutions, but its wide bandgap (2.7 eV) limits its light harvesting efficiency (LHE) to about 12% of the solar spectrum.^[8,9] On the other hand, BiVO_4 is a ternary metal oxide with a narrow bandgap (2.4 eV),^[10] but poor charge separation and surface kinetics hinder its PEC performance.^[11]

Thus, by building a $\text{WO}_3/\text{BiVO}_4$ heterojunction, WO_3 controls the transport properties and enhances the poor charge extraction of BiVO_4 , by promoting the injection of photogenerated electrons from BiVO_4 to WO_3 and suppressing bulk recombination. On the other hand, BiVO_4 provides enhanced photon collection in the visible region, up to ≈ 500 nm.^[12,13]

The poor surface kinetics of OER on BiVO_4 can be further improved by depositing OER catalyst. Prussian blue (PB)-type materials are promising alternatives to noble metals-based catalysts (Ir or Ru), which are the benchmark for OER catalysis.^[14] These inorganic complex salts are easily produced by soft chemistry methods^[15] and are stable within a very large pH range.^[16] Among them, CoFe–PB showed a remarkable increase in photocurrent, lower photoanodic onset potentials, and excellent stability when coupled with BiVO_4 .^[3]

To further improve the design of PEC devices for solar fuel production, it is necessary to understand the properties and

limitations of each material or junction with regard to the key optoelectronic processes, namely, 1) exciton generation upon light absorption, 2) charge separation and bulk transport, 3) charge transfer at the semiconductor–electrolyte interface.

Among various spectroscopic and electrochemical techniques available to explore the dynamics of PEC interfaces, operando techniques are most valuable, because they provide information about the behavior of the system upon external stimuli, such as illumination, applied bias, and chemical environment.

Electrochemical impedance spectroscopy (EIS) is a powerful technique to probe the electrical properties of photoelectrodes in the dark, but, for their characterization under light stimulus, modeling through an electrical equivalent circuit that describes the relevant physical processes occurring within the material is required. In the presence of multiple competing processes and complex interfaces, which are often found in PEC systems, the construction of an electrical model can be difficult, as the frequency response of the PEC system may depend on several interlaced resistive and capacitive contributions, which are sometimes difficult to separate or interpret in an unambiguous fashion. Even though EIS is widely used to study the capacitive response of semiconductor/electrolyte interfaces, the characterization of the relevant kinetic processes occurring at heterojunctions and semiconductor/electrolyte interfaces can be more effectively carried out by intensity-modulated photocurrent spectroscopy (IMPS). The basic idea of IMPS is to analyze, as a function of frequency, the amplitude and phase of the photocurrent generated by the system in response to a sinusoidal modulation of the incident light intensity, which perturbs the surface concentration of the photogenerated carriers.^[17–19]

In this work, the charge carrier dynamics of a WO₃/BiVO₄/CoFe–PB heterojunction, used in a conventional three-electrode cell for water splitting, has been studied using IMPS. To gain a detailed and consistent picture of the processes occurring at such a complex PEC interface, the behavior of WO₃/BiVO₄/CoFe–PB heterojunction was compared with pristine colloidal WO₃ and WO₃/BiVO₄ heterojunctions with and without the addition of a CoFe–PB catalyst. In particular, after a complete structural and functional characterization of these photoanodes, we applied an innovative approach to investigate the photoinduced carrier dynamics: this technique is based on the implementation of wavelength-dependent IMPS (WD-IMPS) analysis, which selectively probes each different layer of the proposed heterojunction and identifies its electron transport properties in the bulk and at the interface. Thus, this methodology offers the ability to separate and address the role of each active component within a complex interface and represents a valuable tool for improving the understanding of dynamic processes relevant to PEC water splitting.

2. Results and Discussion

2.1. Structure, Morphology, and Optical Properties

Morphological characterization of the photoanodes is reported in **Figure 1**. Colloidal WO₃ (**Figure 1a**) is characterized by a nanostructured morphology made of aggregated nanoparticles with

an average diameter of 45 ± 12 nm, sintered together in a porous 3D network. After the electrodeposition of BiVO₄ on WO₃ (**Figure 1b**), a homogeneous thin layer appears on the WO₃ nanoparticles, increasing the average size to 52 ± 8 nm. Finally, the addition of CoFe–PB catalyst results in homogeneous coating on top of BiVO₄ (**Figure 1c**). High-resolution transmission electron microscopy (HRTEM) micrographs of the WO₃/BiVO₄/CoFe–PB heterojunction display crystalline nanoparticles with *d*-spacing compatible with monoclinic WO₃ (**Figure 1e,f**). Interestingly, the surface of WO₃ colloids did not display a homogeneous compact layer of BiVO₄ nanoparticles (**Figure 1g**) but rather small (<10 nm) BiVO₄ nanocrystals. While their crystal structure cannot be fully resolved due to beam sensitivity-related instability, the observed interplanar spacings are compatible with distorted scheelite BiVO₄. The average composition obtained by energy-dispersive spectrometry (EDS) analysis in scanning electron microscopy (SEM) is reported in **Figure S1**, Supporting Information, while the local composition and the distribution of CoFe–PB catalyst are further illustrated by the scanning transmission electron microscopy (STEM)–EDS maps in **Figure S2**, Supporting Information, displaying homogeneous distribution both on BiVO₄ and on WO₃ layers.

Figure 1d shows the X-Ray diffraction (XRD) profiles of the three photoanodes. In agreement with the above HRTEM analysis, WO₃ films exhibit a monoclinic structure, while BiVO₄ films show the typical monoclinic clinobisvanite structure (distorted scheelite structure), as previously reported.^[20] The WO₃ peak intensities are the same in all the photoanodes, and the reflections associated to BiVO₄ are much lower in intensity than those corresponding to WO₃ due to the different thicknesses of the two layers. The addition of the catalyst does not modify the XRD profile, as expected for a very thin overlayer.

Figure 2 displays the optical absorbance spectra of the WO₃ film and of the WO₃/BiVO₄ heterojunction, with and without the CoFe–PB catalyst. The spectra are in good agreement with the nominal bandgap energies for WO₃ and BiVO₄, respectively, about 2.7 eV (440 nm) and 2.4 eV (510 nm).^[9,10,21,22] The catalyst does not add any significant contributions to the absorption properties of the material in the considered wavelength range. Due to the minor transmittance of the heterostructure in the UV region, the contribution of WO₃ to the absorption spectrum was not observed in the corresponding samples, as frequently reported in similar samples.^[12]

As later discussed in the IMPS results analysis, two different monochromatic light emitting diodes (LEDs) were used to analyze the carrier dynamics of the photoanodes, to selectively excite either the BiVO₄ layer or the whole photoanode. The LEDs have nominal peak wavelengths of 470 and 370 nm and are referred in the text as blue and UV LED, respectively. From the absorbance *A*, LHE was calculated using the formula

$$\text{LHE} = 1 - 10^{-A(\lambda)} \quad (1)$$

defined as the fraction of light intensity absorbed by the material at each wavelength. The LHE spectrum and the corresponding value at the nominal LED wavelength for the three photoanodes are reported in **Figure S3**, Supporting Information.

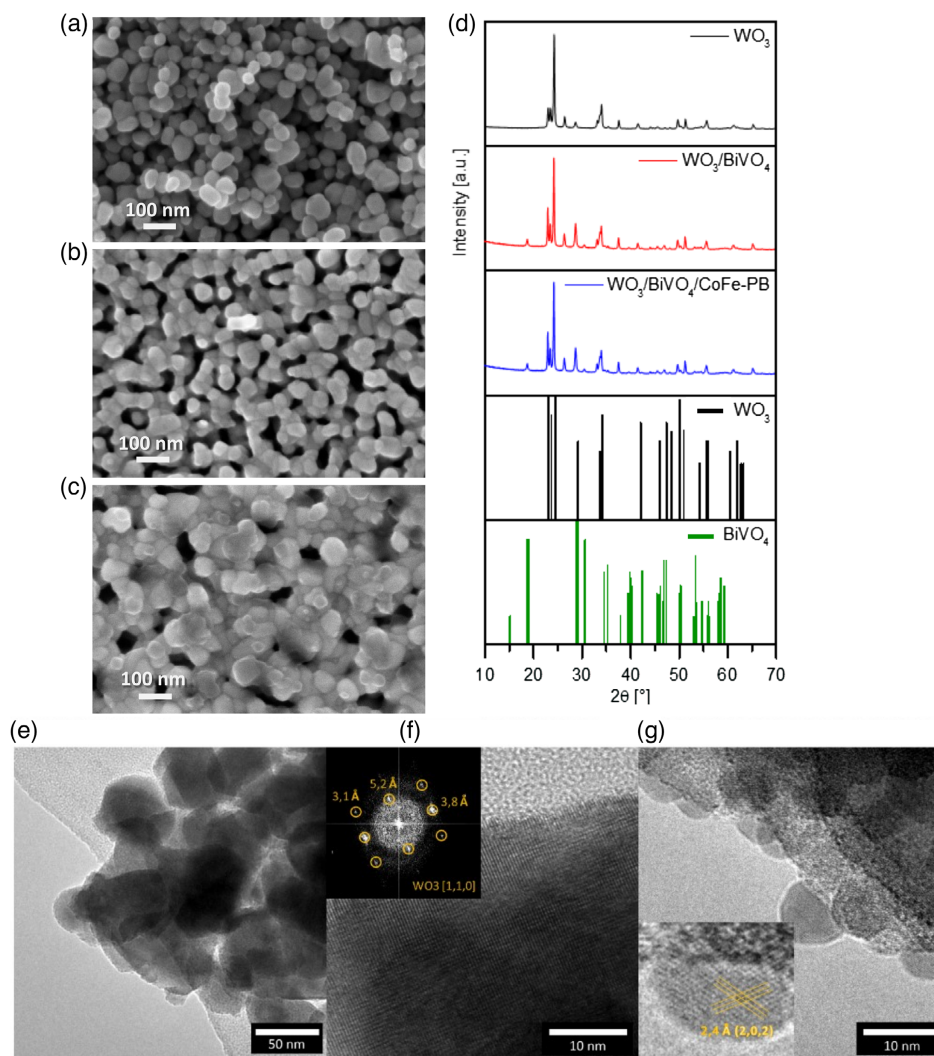


Figure 1. FESEM micrographs of a) WO₃, b) WO₃/BiVO₄, and c) WO₃/BiVO₄/CoFe-PB. d) The XRD pattern of the prepared photoanodes and reference patterns for WO₃ and BiVO₄. e–g) HRTEM micrographs of the WO₃/BiVO₄/CoFe-PB sample. In the inset: f) Fast Fourier transform displaying the crystal pattern of monoclinic WO₃, oriented on [1,1,0] zone axis. g) Higher-magnification detail of a BiVO₄ nanoparticle.

2.2. PEC Characterization

The electrochemically active surface area (ECSA) of the WO₃ film gives an estimation of the real surface area involved in the PEC processes, and it was extracted from EIS data at open-circuit potential (Figure S5, Supporting Information) and from Mott–Schottky measurements (Figure S6, Supporting Information) on the WO₃ photoanode in the dark. The ECSA was estimated ≈ 24 times higher than that of a flat electrode (further details on the calculation are reported in Supporting Information), and therefore WO₃ can be considered as mesoporous.^[14,23–25] The addition of BiVO₄ and CoFe-PB on the surface of WO₃ does not significantly modify the morphology of the photoanode surface, as suggested by SEM and TEM analysis; thus, the whole structure can be considered mesoporous as well.

Figure 3a shows the linear sweep voltammetry (LSV) curves measured in acetate solution under chopped white LED

illumination, with an incident intensity of 1 sun. Important contributions of the BiVO₄ layer and of the CoFe-PB catalyst can be noticed with respect to bare WO₃. The deposition of BiVO₄ on colloidal WO₃ enhances more than four times the maximum photocurrent (1.85 mA cm^{-2} at $1.7 V_{\text{RHE}}$) and shifts the onset toward more positive potentials, requiring a stronger anodic polarization to reach the saturation photocurrent. The deposition of CoFe-PB on top of the heterojunction further increases the photocurrent density, up to almost 2.5 mA cm^{-2} . Moreover, the onset is shifted back to more cathodic potentials, approaching the one observed in pristine WO₃, as already reported in previous works on similar junctions.^[3] The current peak observed at $0.4 V_{\text{RHE}}$ is related to the reoxidation of W(V) to W(VI)^[26]: W(V) is generated during the *J*–*V* experiment upon scanning the electrode at $V < 0.7 V_{\text{RHE}}$ and requires charge compensation, here, in the form of Na⁺, by the electrolyte. When BiVO₄ and the catalyst are present, this effect is reduced but

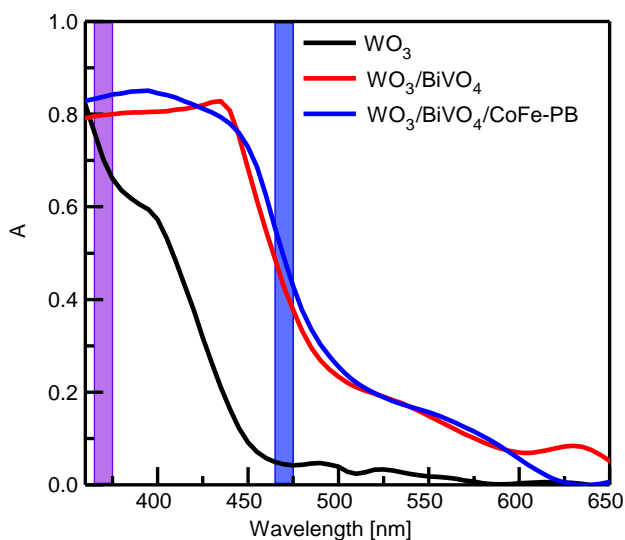


Figure 2. Absorbance spectra of the three studied photoanodes. LED wavelengths are highlighted with the corresponding color.

it does not disappear completely; this might be an indication that the WO_3 layer is not completely covered, consistently with the morphological results, and some of the W(VI) ions may still undergo electrochemical reduction at the relevant voltage.

Figure 3b shows the incident photon-to-current conversion efficiency (IPCE) spectra of the three electrodes under an applied potential of $1.7 V_{\text{RHE}}$. WO_3 has a high IPCE (up to 35%) in the UV region of the spectrum, whereas the IPCE is almost zero for $\lambda > 450 \text{ nm}$, as expected as the bandgap is 2.7 eV . When the BiVO_4 layer is added, the IPCE is extended toward the visible range, up to $\approx 525 \text{ nm}$. However, the IPCE of pristine WO_3 exceeds the one of the heterojunction in the UV region ($< 390 \text{ nm}$). Upon addition of CoFe-PB catalyst, the IPCE increases both in the UV and visible region of the spectrum. As

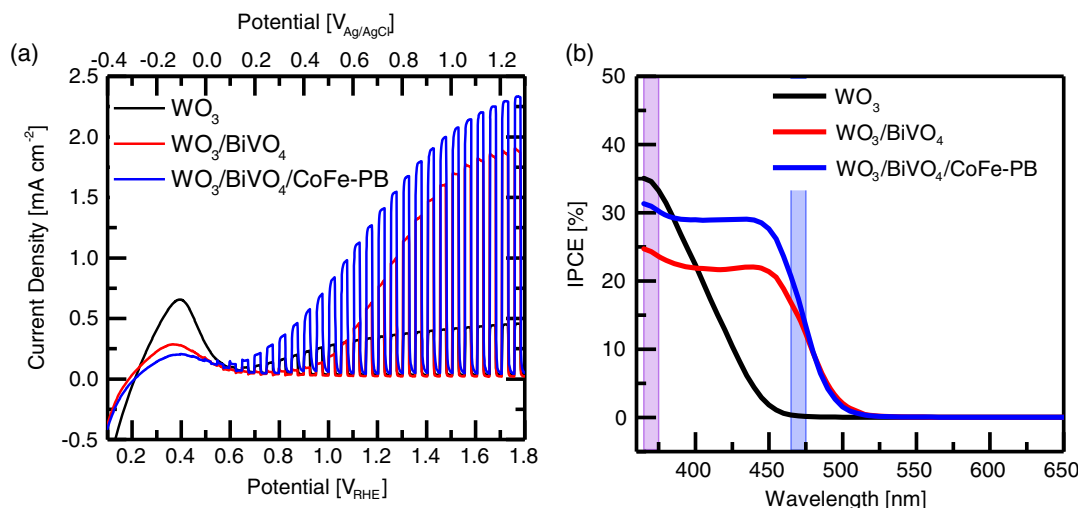


Figure 3. a) Chopped LSV under 1-sun equivalent illumination in acetate buffer solution (pH 5) and b) IPCE spectra at $1.7 V_{\text{RHE}}$ for WO_3 , $\text{WO}_3/\text{BiVO}_4$, and $\text{WO}_3/\text{BiVO}_4/\text{CoFe-PB}$ samples. The colored superimposed stripes represent the monochromatic LED wavelengths used for IMPS analysis.

the catalyst does not modify the absorption properties of the electrode, this spectral responsivity enhancement suggests that the catalyst either boosts the separation efficiency of photogenerated carriers or suppresses their recombination at the surface, or both. However, the conversion efficiency given by IPCE is extracted only from the steady-state photocurrent: to gather information on the carrier dynamics out of equilibrium, we turn to WD-IMPS.

The IMPS complex transfer function $Y(\omega)$ is calculated from the ratio between the amplitude of the modulated photocurrent j_{ph} and the amplitude of the AC incident photon flux I_{inc} . Following the work of Gutiérrez et al.,^[27] j_{ph} can be divided by the electron charge e and the intensity can be divided by hc/λ , so that they are expressed in electrons $\text{cm}^{-2} \text{s}^{-1}$ and in photons $\text{cm}^{-2} \text{s}^{-1}$, respectively.

$$Y(\omega) = \frac{j_{\text{ph}}(\omega)}{I_{\text{inc}}(\omega)} \cdot \frac{hc}{\lambda e} \quad (2)$$

where ω is the frequency of the modulation and λ is the wavelength of the incident photon.^[19] The normalized $Y(\omega)$ is a quantity that describes the number of charge carriers divided by the number of incident photons and contains information on the efficiency of the photoelectrode.

Usually, for n-type semiconductor, the IMPS response gives rise to two complex plane loops, as shown in **Figure 4**: a negative semicircle in the fourth quadrant related to the high-frequency range and fast charge transfer processes and a positive semicircle in the first quadrant related to low frequencies and slower processes. The negative semicircle is determined by the charge transport inside the photoelectrode. At sufficiently low frequencies, the modulated photocurrent is in phase with light modulation, implying that charge separation is achieved, so the intercept of Y with the real axis is (see Figure 4)

$$Y'_{\text{int}} = \text{LHE} \times \text{CSE} \quad (3)$$

where CSE is the charge separation efficiency, defined as the ratio between the holes that reach the semiconductor–electrolyte

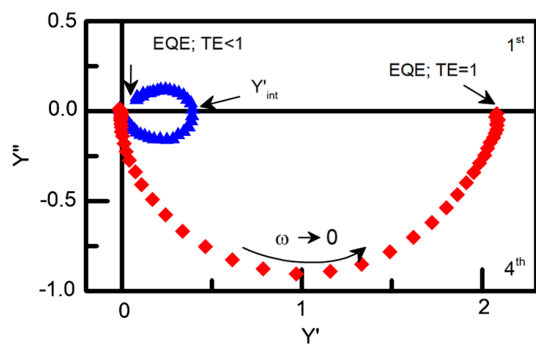


Figure 4. Examples of IMPS spectra at different applied potentials. The blue plot shows the behavior at low applied potentials, where a loss of EQE is present due to a low TE. The red plot shows the behavior at high potentials where surface recombination becomes negligible and the TE is assumed to be 1.

interface and the number of photogenerated electron–hole pairs. In other words, CSE represents the percentage of photogenerated holes that are available for oxidation reactions and provides information on the transport properties of the material. This is true only if the charge transfer and surface recombination processes are slower than charge separation, so that charge separation is limited by bulk recombination.

The positive semicircle appears if the time constant related to charge separation is significantly smaller, and the quantum efficiency is determined by the balance of surface recombination and charge transfer rates at the electrode/electrolyte junction: the ratio between the intercepts of the two different loops with the real axis is the transfer efficiency (TE), which is the number of holes that can oxidize water divided by the number of holes that were successfully separated inside the electrode. Finally, the intercept of the positive semicircle at the lowest frequency corresponds to the external quantum efficiency (EQE). Therefore, the overall efficiency of the photoelectrode is

$$\text{EQE} = \text{LHE} \times \text{CSE} \times \text{TE} \quad (4)$$

The EQE is the ratio between the number of holes transferred to the electrolyte and the number of absorbed photons. Thus, from a single IMPS measurement, it is possible to extract information on bulk transport processes and surface recombination processes of the photoelectrode.

If the positive semicircle loops back to the origin (blue plot in Figure 4), this means that surface recombination is much faster than hole scavenging; consequently, all the photogenerated charges recombine and $\text{EQE} = 0$. If the positive semicircle is absent (red plot in Figure 4), it means that the charge transfer is much faster than surface recombination and the EQE is governed essentially by the rate of hole transfer to the solution. In this latter case, other features might be observed: when the cell time constant is close to the charge separation time constant, two superimposed semicircles possibly merging in one distorted semicircle appear in the complex plane; if the charge separation is much faster, the spectrum results in one symmetrical semicircle.^[27]

A distortion in the lower loop is observed also if full charge separation is not attained, but this can be used only to describe qualitatively the charge transfer processes at low frequencies of modulation, as the implementation of a quantitative model would need a too large number of parameters.

Figure 5 shows the IMPS spectra of the three samples under UV and blue monochromatic illumination and at different applied potentials. We used only the UV LED for WO_3 , which does not absorb the blue LED wavelength. For $\text{WO}_3/\text{BiVO}_4$ and $\text{WO}_3/\text{BiVO}_4/\text{CoFe-PB}$, the use of both blue and UV LEDs makes it possible to selectively excite the different layers of the photoanode, thus identifying the role of each material with respect to the heterojunction PEC activity. The intensity of the DC illumination bias used in each measurement was chosen to have the same steady-state photocurrent of $35.4 \mu\text{A cm}^{-2}$, thus avoiding any dependence of the involved charge carrier processes on the photocurrent density and allowing a more meaningful comparison between the different electrodes. The intensity of the AC amplitude component was 10% of the DC signal intensity. The value of the intensity of the monochromatic DC illumination bias has the same order of magnitude used in other works on similar electrodes^[28] and is close to the monochromatic component of the Xe lamp used during IPCE measurements (Figure S7, Supporting Information). Figure S8, Supporting Information, compares two IMPS spectra where the DC illumination bias was given by a white LED with incident intensity of 1 sun or by the blue LED, to ensure that our discussion can be actually representative of the work conditions of the photoanode under 1 sun illumination.

The first row of Figure 5 shows the IMPS spectra of the WO_3 photoanode. Upon UV excitation, only the negative semicircle is present, meaning that surface recombination is much slower than charge transfer from the electrode to the solution.

On the other hand, the IMPS spectra of $\text{WO}_3/\text{BiVO}_4$ photoanodes show positive semicircles, indicating surface recombination up to $1.1 V_{\text{RHE}}$, that disappears at more anodic potentials for both used light sources, in agreement with another work on BiVO_4 .^[28] The only difference between UV and blue illumination is given by the value of real-axis intercepts, which is related to the efficiency of the electrode and is commented later. Adding the CoFe–PB catalyst does not change much the shape of the spectra compared with the bare $\text{WO}_3/\text{BiVO}_4$ photoanode, but the recombination semicircle disappears at a lower applied potential (0.9 vs $1.1 V_{\text{RHE}}$), consistent with the more cathodic photocurrent onset previously discussed.

The distortion observed in the lower loop at low frequencies might be related to the surface chemistry of the photoanodes upon water photo-oxidation, as the generation of hydroxyl and peroxide moieties might introduce traps that slow down the charge transport in the photoanode.^[27] The distortion is less evident in the spectra of the $\text{WO}_3/\text{BiVO}_4/\text{CoFe-PB}$ photoanode and this suggests that the presence of the catalyst reduces the effect of surface poisoning.

From the IMPS data, we can now extrapolate the relative efficiency of each optoelectronic process taking place in the PEC cell.

The CSE versus applied potential is reported in the left column of **Figure 6**. Upon blue excitation, the CSE of $\text{WO}_3/\text{BiVO}_4$ displays a sigmoidal shape with onset about $0.9 V_{\text{RHE}}$ and maximum

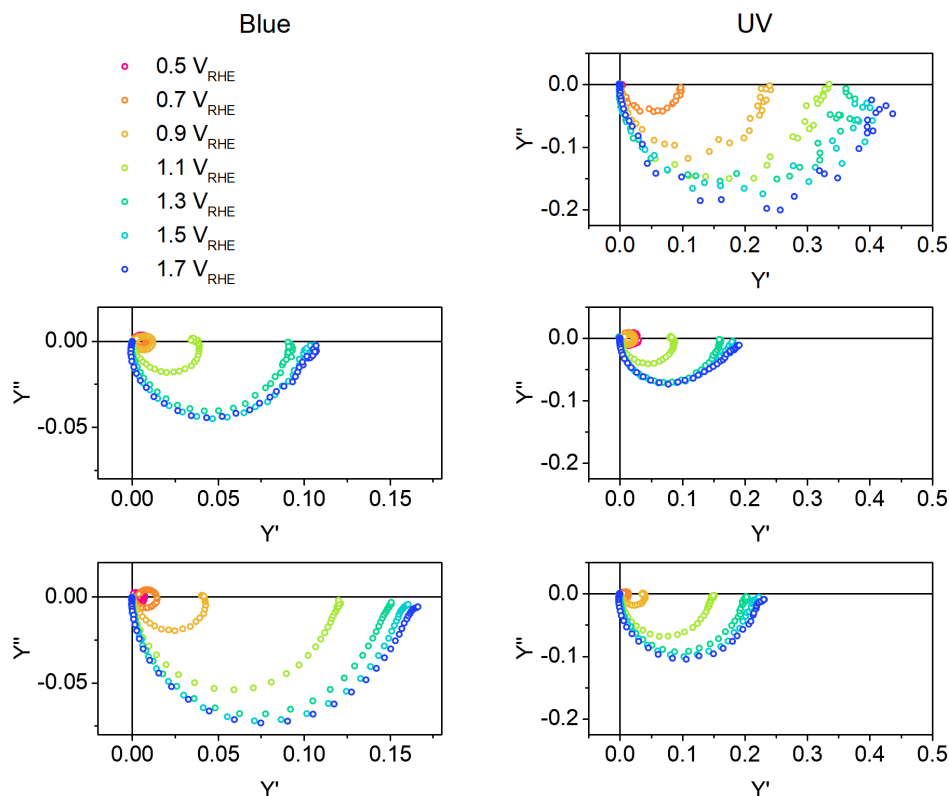


Figure 5. IMPS response of the photoanodes under UV/blue illumination (producing steady-state photocurrent = $35.4 \mu\text{A cm}^{-2}$) in 0.2M acetate buffer solution (pH 5).

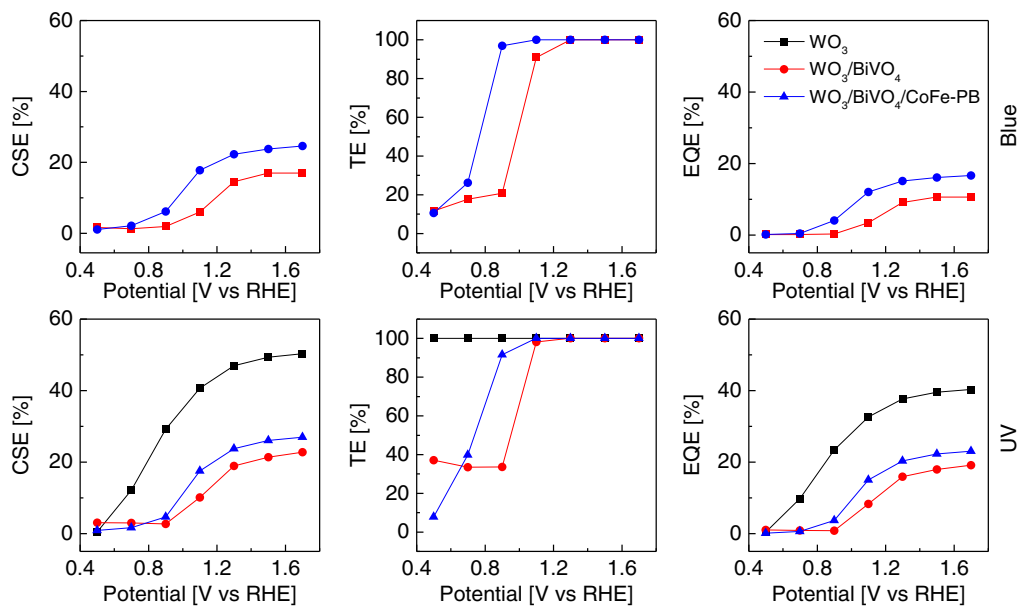


Figure 6. CSE, TE, and EQE of the WO_3 , $\text{WO}_3/\text{BiVO}_4$, and $\text{WO}_3/\text{BiVO}_4/\text{CoFe-PB}$ photoanodes when illuminated with the blue (top row) and UV (bottom row) LEDs.

CSE value in the high-polarization regime ($1.5 V_{\text{RHE}}$) is around 17%. A similar trend is observed in $\text{WO}_3/\text{BiVO}_4/\text{CoFe-PB}$, but the CSE values display a 50% enhancement. In this model, the CSE describes only transport processes inside the bulk and is

independent of the light absorption properties or surface processes, so we infer that the presence of the catalyst significantly improves the bulk electron-hole separation, especially for potential above $0.9 V_{\text{RHE}}$.

Under UV light, the WO_3 photoanode shows the highest CSE, as it reaches values around 50%. Therefore, it appears that the presence of the BiVO_4 layer partly reduces the collection of charges photogenerated within WO_3 . As with blue excitation, also under UV light, we notice a 20% enhancement of CSE upon addition of the CoFe–PB catalyst in the potential region above $0.9 V_{\text{RHE}}$.

Moving to the analysis of the TE, while pristine colloidal WO_3 exhibits unitary TE in the whole used potential window upon UV illumination, the addition of the BiVO_4 layer introduces superficial recombination at potentials lower than $1 V_{\text{RHE}}$, with all excitation sources. Thus, BiVO_4 in the low-potential regime is less efficient than WO_3 in transferring charges to the solution, meaning that the number of holes that effectively oxidize water decreases because of competing recombination. This is consistent with the shifted photoanodic onset of the $\text{WO}_3/\text{BiVO}_4$ junction with respect to bare WO_3 . Indeed, only when reaching a sufficiently strong anodic polarization, electrons are drawn away from BiVO_4 and the electron/hole recombination process at the surface becomes negligible. On the other hand, the addition of the CoFe–PB catalyst shifts the onset of the TE to less anodic potentials, partially compensating the detrimental effect resulting from BiVO_4 -related recombination centers. The catalyst has therefore the beneficial effect of reducing surface recombination at low applied potentials by increasing the hole transfer rate from the electrode to the solution, as previously suggested.^[3,29]

However, the increased charge transfer rates may explain the catalyst-related shift of the photocurrent onset, but fails to elucidate the photocurrent enhancement in the high-polarization regime, where the TE is the same for all photoanodes and independent of the illumination wavelength.

The EQE versus the applied potential is shown in the right column of Figure 6. With blue LED, the catalyst slightly increases the saturation EQE from 10.6% to 16.6%, with a cathodic shift of 0.2 V. Upon UV illumination, the EQE of $\text{WO}_3/\text{BiVO}_4$ is boosted by CoFe–PB, increasing from 19% to 23%. UV-excited bare WO_3 displays a higher EQE in the whole potential range with respect to the $\text{WO}_3/\text{BiVO}_4$ heterostructure irrespective of the presence of the catalyst. The IPCE measured at $1.7 V_{\text{RHE}}$ is in good agreement with the EQE extracted by IMPS spectra at equivalent potential with the corresponding excitation wavelength, validating the theoretical model used to extract these efficiencies from the IMPS measurements. Compared with IPCE, IMPS allows to discern the contribution of each process to the steady-state EQE by resolving the carrier dynamics, revealing whether the EQE is limited by the charge separation in the bulk or by the charge transfer at the interface.

2.3. Efficiency Loss at the Heterojunction

The proposed data treatment highlight three critical points, namely, 1) while the EQE of the heterojunction is largely improved in the visible range, where one of pristine WO_3 is negligible due to the lack of light absorption, the opposite is observed in the UV region, where EQE is lower in the heterojunction compared with pristine WO_3 ; 2) the CSE of the heterojunction is enhanced by the deposition of CoFe–PB catalyst, and 3) the

TE drop observed in the low-polarization regime in the presence of BiVO_4 is partially recovered by the addition of the catalyst, while in the high-polarization regime, the TE is unitary for all samples.

With respect to the first point, the EQE drop of the heterojunction in the UV range might result from either the inner filter effect of the BiVO_4 layer, shadowing the incident light on the underlying WO_3 , or the rise of recombination processes related to the heterojunction, or both. To determine the detrimental role of both mechanisms on the EQE in the UV excitation regime, the overall EQE of the heterojunction, at a specific potential, might be assumed to be resulting from the sum of the contributions of each layer, depending on the relative CSE, LHE, and TE, as discussed in the SI. As a result, the inner filter effect may be estimated to contribute to $\approx 20\%$ of the EQE decrease of the heterojunction in the UV region, while the residual loss is related to the e–h pairs generated in the WO_3 layer recombining at the heterojunction interface. To describe these processes, we can introduce an interface recombination term $R_{\text{int,het}}$ defined as

$$\text{CSE}_{\text{WO}_3(\text{het})} = \text{CSE}_{\text{WO}_3} \times (1 - R_{\text{int,het}}) \quad (5)$$

The resulting $R_{\text{int,het}}$ as a function of the potential in $\text{WO}_3/\text{BiVO}_4$ is shown in Figure 7 (red line), displaying a sigmoidal shape with onset at about $0.9 V_{\text{RHE}}$. In the $\text{WO}_3/\text{BiVO}_4$ electrode, as part of the electroactive WO_3 surface could be directly contacted by the electrolyte, we would expect the occurrence of direct hole-scavenging pathways from WO_3 to the liquid phase, but the high $R_{\text{int,het}}$ of the heterojunction for potentials lower than $0.9 V_{\text{RHE}}$ suggests that the large majority of holes generated inside WO_3 are instead lost due to interfacial recombination with BiVO_4 . For higher applied potentials, $R_{\text{int,het}}$ rapidly decreases, probably due to the stronger depletion field built at the $\text{WO}_3/\text{BiVO}_4$ junction facilitating the separation of the charge carriers, transport of the photogenerated holes to the valence band (VB) of BiVO_4 , and the injection in the electrolyte. It is however interesting to observe that even when the $R_{\text{int,het}}$ plateau is reached in the high-polarization regime ($1.7 V_{\text{RHE}}$), its minimum value is 53%, corresponding to the fraction of photogenerated

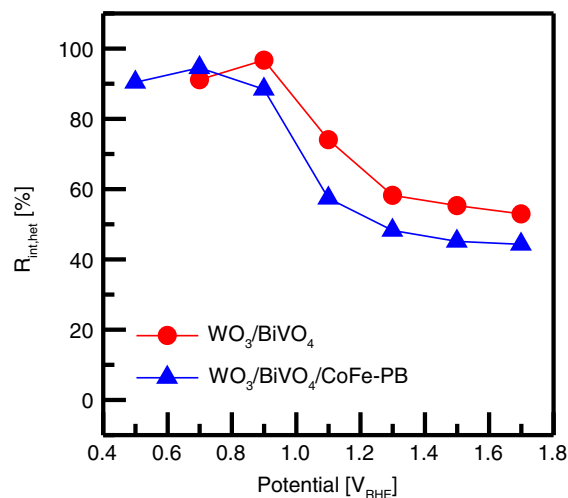


Figure 7. $R_{\text{int,het}}$ in $\text{WO}_3/\text{BiVO}_4$ and $\text{WO}_3/\text{BiVO}_4/\text{CoFe-PB}$ photoanodes.

holes recombining at the $\text{WO}_3/\text{BiVO}_4$ interface, before being effectively transferred across the heterojunction. Upon addition of CoFe–PB, $R_{\text{int,het}}$ displays the same potential-dependent behavior, but the minimum value decreases to about 44% ($1.7 V_{\text{RHE}}$), pointing out a positive influence of the catalyst on the charge separation process (Figure 7, blue line).

Furthermore, the addition of the catalyst has a notable impact on the CSE and TE of BiVO_4 , both in the UV and visible region of the solar spectrum. We observe that CoFe–PB improves the transfer of holes to the solution at low potentials, but at more anodic potentials, where the recombination of BiVO_4 at the semiconductor/electrolyte interface is already negligible, the catalyst mainly affects the CSE within the BiVO_4 layer. While this is counterintuitive, as catalysts are generally expected to affect mainly the TE, a similar behavior was previously observed in the work of Moss et al.^[29] using more complex multiscale time-resolved spectroscopy. Consistent with our analysis, CoFe–PB was found to enhance charge collection compared with pristine BiVO_4 due to catalyst-related suppression of

recombination losses at the surface of the BiVO_4 layer, whereas the charge TE to the electrolyte was not significantly improved. We may suggest that the main role of the catalyst in this case is to scavenge holes from the valence band of BiVO_4 , effectively separating them from electrons, rather than increasing the kinetics of water oxidation. The microscopic nature of the $\text{BiVO}_4/\text{CoFe-PB}$ interface is likely to play a role in favoring the scavenging process and deserves deeper investigations.

Figure 8 schematically summarizes the carrier dynamics of the studied photoanodes by shining either UV or blue light on them. Charge generation induced by photon absorption is described by red arrows, occurring in different layers, depending on the excitation wavelength, while black arrows represent charge migration processes within each semiconductor and across the heterojunction. Yellow arrows represent the recombination at the heterojunction, previously described as $R_{\text{int,het}}$, and blue arrows represent the recombination processes taking place at the BiVO_4 surface, strongly reduced by the presence of CoFe–PB catalyst.

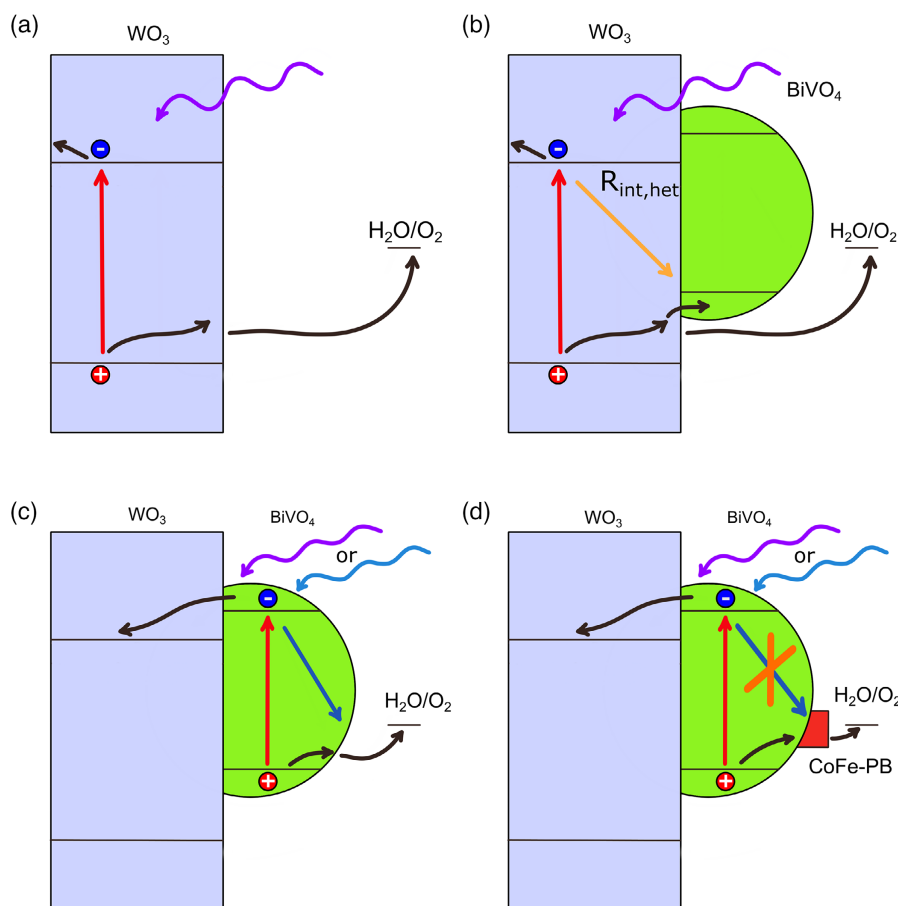


Figure 8. Schematics of the charge carrier dynamics in the a) WO_3 , b–c) $\text{WO}_3/\text{BiVO}_4$, and d) $\text{WO}_3/\text{BiVO}_4/\text{CoFe-PB}$ samples, reporting the main recombination pathways and the effect of the CoFe–PB catalyst on them: (a) the charges generated (red arrow) by WO_3 upon UV light absorption are separated (black arrows) and the holes are transferred into the solution; (b) when BiVO_4 is added, part of the generated holes is transferred from the VB of WO_3 to the VB of BiVO_4 : here the recombination at the $\text{WO}_3/\text{BiVO}_4$ heterojunction limits the hole transfer and reduces the CSE of the layer; (c) BiVO_4 is able to absorb both UV and blue photons, but the CSE is limited by the poor transport properties of the material and recombination at the surface (blue arrow); (d) the CSE enhancement revealed by IMPS after the addition of CoFe–PB is due to hole transfer to the catalyst, which reduces recombination losses at the BiVO_4 surface, in agreement with the time-resolved pump-probe study of Moss et al.^[29]

3. Conclusion

The present article establishes WD-IMPS as a powerful technique for a straightforward investigation of semiconductor photoelectrodes' optoelectronic properties in operando PEC cells. The proposed data analysis, exploiting the information resulting from the selective excitation of different layers of heterojunctions, allows for a deep understanding of the loss mechanisms affecting the charge extraction from the semiconductors. Indeed, by isolating the contribution of the photoinduced charge carriers generated by a single semiconductor, the use of multiple-wavelength IMPS analysis shows the occurrence of the recombination process at the heterostructure interface to be identified.

By applying this approach to the $\text{WO}_3/\text{BiVO}_4/\text{CoFe-PB}$ heterojunction, we identified the occurrence of interface recombination processes affecting the semiconductor junction, as well as the positive contribution of the inorganic complex catalyst on the charge separation efficiency of the BiVO_4 layer. WD-IMPS therefore provides thorough and reliable information on the charge carrier dynamics in complex heterostructures, probing the operando behavior of a photoelectrode with simple, widely available facilities.

4. Experimental Section

Preparation of the Heterojunction: Chemicals and solvents were purchased from Merck, Alfa Aesar, and Carlo Erba and were used as received. Water used for material preparations was deionized through a Millipore system.

FTO/ WO_3 Electrodes: The preparation of spin-coated WO_3 films constituted by WO_3 nanoparticles was done according to previous literature.^[8,30] Briefly, the preparation of colloidal WO_3 was first accomplished by precipitating a H_2WO_4 gel by addition of concentrated HCl to aqueous Na_2WO_4 (Alfa Aesar, $\geq 99\%$). After several washings of H_2WO_4 carried out by redispersion/centrifugation, a stable H_2WO_4 sol was generated by peptization with oxalic acid (Alfa Aesar $\geq 99.5\%$) at 60°C . The resulting colloidal suspension (having an overall mass of 8–8.5 g in the typical preparation) was densified by adding 20% w/w Carbowax (Sigma-Aldrich) and a few drops of Triton X-100 (Fluka), to improve the colloid spreadability during the subsequent FTO-coating process. Dry nanoparticulate films (colloidal photoanodes) were obtained onto the well-cleaned FTO glass (Pilkington TEC 7) by spin coating the H_2WO_4 aqueous colloidal precursor described earlier. In the study herein reported, six WO_3 layers were sequentially deposited, each layer being thermally annealed at 550°C for 30 min in air before the deposition of the next one. The total thickness of the electrode was $1\ \mu\text{m}$, as shown in Figure S9, Supporting Information.

FTO/ $\text{WO}_3/\text{BiVO}_4$ Electrodes: Deposition of BiVO_4 on WO_3 photoanodes supported by FTO was achieved according to a previously published procedure,^[22] inspired by an electrochemical methodology developed by Seabold et al.^[31] Briefly, 10 mM $\text{Bi}(\text{NO}_3)_3$ (Sigma Aldrich $\geq 99\%$) was slowly added to an acidic solution of 10 mM VOSO_4 (Alfa Aesar, 99.9%). Dropwise addition of concentrated HNO_3 over a 30 min period was necessary to achieve the complete dissolution of $\text{Bi}(\text{NO}_3)_3$. After this point, the pH was rapidly increased to 4.5 using 2M CH_3COONa (Alfa Aesar 99%). The resulting solution was quickly used as an electrolyte for two-electrode potentiostatic electrodeposition by applying 210 mV between FTO/ WO_3 and a platinum foil at room temperature for 300 s. The typical distance between the FTO/ WO_3 working electrode and the Pt foil was $\approx 3\ \text{mm}$. After deposition, the resulting FTO supported photoanode was abundantly rinsed with water, dried at room temperature, and finally annealed at 500°C in air for 2 h.

FTO/ $\text{WO}_3/\text{BiVO}_4/\text{CoFe-PB}$: Cobalt-iron Prussian blue catalyst (CoFe-PB)^[3] was deposited by surface ionic layer adsorption and reaction

(SILAR) at room temperature. Each deposition cycle was carried out as follows: first, the FTO/ $\text{WO}_3/\text{BiVO}_4$ electrode was dipped in a 0.02M $\text{K}_3[\text{Fe}(\text{CN})_6]$ (Riedel de Haen 99%) solution for 10–15 min while gently magnetically stirring the solution; this was followed by rinsing the electrode with water and immersion in 0.04M CoCl_2 (Carlo Erba, 99%) for another 10–15 min under stirring. After washing out the $\text{Co}(\text{II})$ excess, this sequence was repeated for four times. The resulting FTO/ $\text{WO}_3/\text{BiVO}_4/\text{CoFe-PB}$ electrodes were then blow dried with warm air and stored in the dark at room temperature before use.

Structural and Optical Characterization: SEM images were collected on a Zeiss LEO 1430 field emission scanning electron microscope (FESEM). HRTEM and scanning transmission electron microscopy–high angle annular dark field (STEM–HAADF) characterization were performed on a FEI Tecnai F20, operating at 200 kV and equipped with EDAX Phoenix spectrometer with an ultrathin window detector for EDS.

XRD patterns were recorded using a PANalytical X'Pert Pro automated diffractometer, equipped with an X'celerator multielement solid-state detector. The diffractometer was operated in Bragg–Brentano $\theta/2\theta$ para-focusing geometry using Ni-filtered $\text{Cu K}\alpha$ radiation.

Absorption spectra were calculated as follows.

$$A = -\log(T + R) \quad (6)$$

where T is the optical transmittance, measured using a Osram 150 W xenon arc lamp coupled with a monochromator (Oriol Instruments) and Si photodiode (Hamamatsu), and R is the diffuse reflectance, measured with a Jasco V-750 UV–vis spectrophotometer, equipped with an integration sphere for absolute reflectance measurements.

PEC Characterization: LSV curves, IPCE, EIS, and IMPS spectra of the photoanodes were measured in a PEC cell with a PGSTAT204 electrochemical workstation, using a three-electrode configuration with a Pt counter electrode and Ag/AgCl electrode as the reference. The electrolyte was a 0.2 M acetate solution ($\text{pH} = 5$). The electrodes were illuminated from the front in all the measurements in the PEC cell and the exposed area was $0.283\ \text{cm}^2$. The LSV curves were acquired with a scan rate of $25\ \text{mV s}^{-1}$, chopping the light with a frequency of 0.5 Hz.

IMPS measurements were performed in the applied bias range of 0.5–1.7 V_{RHE} and frequency range of 0.1 Hz–10 kHz. Two monochromatic LEDs, with nominal wavelengths of 470 nm and 370 nm, were driven by an LED driver (Thorlabs DC2100) to superimpose a modulated illumination to a constant illumination bias. The sinusoidal modulation was about 10% of the illumination bias, to ensure a linear response of the LEDs. Using a beam splitter, the light was divided into two beams, one on the PEC cell to illuminate the sample and the other one on a calibrated Si photodiode (Hamamatsu) to measure the light intensity.

The spectral efficiency of the photoanode for water splitting was found by measuring the photoanodic current with PGSTAT204 as a function of the incident wavelength from 380 to 800 nm in steps of 5 nm. The light source was an Osram 150 W xenon arc lamp and the incident monochromatic irradiance was measured with a calibrated Si photodiode. IPCE was calculated using

$$\text{IPCE}(\lambda) = \frac{j_{\text{ph}}(\lambda)}{I_{\text{inc}}(\lambda)} \cdot \frac{hc}{\lambda e} \quad (7)$$

in which $j_{\text{ph}}(\lambda)$ and $I_{\text{inc}}(\lambda)$ are the steady-state photocurrent density and incident radiant power density, respectively, at wavelength λ .

Supporting Information

Supporting Information is available from the Wiley Online Library or from the author.

Acknowledgements

P.V. and A.P. contributed equally to this work. This project received funding from the European Union's Horizon 2020 research and innovation program under grant agreement no. 101006839 (CONDOR).

Open Access Funding provided by Università degli Studi di Bologna within the CRUI-CARE Agreement.

Conflict of Interest

The authors declare no conflict of interest.

Data Availability Statement

The data that support the findings of this study are available from the corresponding author upon reasonable request.

Keywords

intensity-modulated photocurrent spectroscopy, photoelectrochemistry, Prussian blue, water splitting, $\text{WO}_3/\text{BiVO}_4$

Received: February 2, 2022

Revised: March 26, 2022

Published online: April 30, 2022

- [1] N. S. Lewis, *Science* **2016**, *351*, aad1920.
- [2] D. Kang, T. W. Kim, S. R. Kubota, A. C. Cardiel, H. G. Cha, K.-S. Choi, *Chem. Rev.* **2015**, *115*, 12839.
- [3] F. S. Hegner, I. Herraiz-Cardona, D. Cardenas-Morcoso, N. López, J.-R. Galán-Mascarós, S. Gimenez, *ACS Appl. Mater. Interfaces* **2017**, *9*, 37671.
- [4] D. K. Zhong, S. Choi, D. R. Gamelin, *J. Am. Chem. Soc.* **2011**, *133*, 18370.
- [5] F. F. Abdi, R. van de Krol, *J. Phys. Chem. C* **2012**, *116*, 9398.
- [6] Y. Pihosh, I. Turkevych, K. Mawatari, J. Uemura, Y. Kazoe, S. Kosar, K. Makita, T. Sugaya, T. Matsui, D. Fujita, M. Tosa, M. Kondo, T. Kitamori, *Sci. Rep.* **2015**, *5*, 11141.
- [7] Y. Zhou, L. Zhang, L. Lin, B. R. Wygant, Y. Liu, Y. Zhu, Y. Zheng, C. B. Mullins, Y. Zhao, X. Zhang, G. Yu, *Nano Lett.* **2017**, *17*, 8012.
- [8] V. Cristino, S. Marinello, A. Molinari, S. Caramori, S. Carli, R. Boaretto, R. Argazzi, L. Meda, C. A. Bignozzi, *J. Mater. Chem. A* **2016**, *4*, 2995.
- [9] C. A. Bignozzi, S. Caramori, V. Cristino, R. Argazzi, L. Meda, A. Tacca, *Chem. Soc. Rev.* **2013**, *42*, 2228.
- [10] Z.-F. Huang, L. Pan, J.-J. Zou, X. Zhang, L. Wang, *Nanoscale* **2014**, *6*, 14044.
- [11] Y. Park, K. J. McDonald, K.-S. Choi, *Chem. Soc. Rev.* **2013**, *42*, 2321.
- [12] P. M. Rao, L. Cai, C. Liu, I. S. Cho, C. H. Lee, J. M. Weisse, P. Yang, X. Zheng, *Nano Lett.* **2014**, *14*, 1099.
- [13] X. Shi, I. Herraiz-Cardona, L. Bertoluzzi, P. Lopez-Varo, J. Bisquert, J. H. Park, S. Gimenez, *Phys. Chem. Chem. Phys.* **2016**, *18*, 9255.
- [14] C. C. L. McCrory, S. Jung, I. M. Ferrer, S. M. Chatman, J. C. Peters, T. F. Jaramillo, *J. Am. Chem. Soc.* **2015**, *137*, 4347.
- [15] M. Aksoy, S. V. K. Nune, F. Karadas, *Inorg. Chem.* **2016**, *55*, 4301.
- [16] L. Han, P. Tang, Á. Reyes-Carmona, B. Rodríguez-García, M. Torrén, J. R. Morante, J. Arbiol, J. R. Galan-Mascaros, *J. Am. Chem. Soc.* **2016**, *138*, 16037.
- [17] J. Li, L. M. Peter, *J. Electroanal. Chem. Interfacial Electrochem.* **1985**, *193*, 27.
- [18] L. M. Peter, *Chem. Rev.* **1990**, *90*, 753.
- [19] E. A. Ponomarev, L. M. Peter, *J. Electroanal. Chem.* **1995**, *396*, 219.
- [20] Y. Liu, B. R. Wygant, K. Kawashima, O. Mabayoje, T. E. Hong, S. G. Lee, J. Lin, J. H. Kim, K. Yubuta, W. Li, J. Li, C. B. Mullins, *Appl. Catal. B Environ.* **2019**, *245*, 227.
- [21] A. Kudo, K. Omori, H. Kato, *J. Am. Chem. Soc.* **1999**, *121*, 11459.
- [22] V. Cristino, L. Pasti, N. Marchetti, S. Berardi, C. A. Bignozzi, A. Molinari, F. Passabi, S. Caramori, L. Amidani, M. Orlandi, N. Bazzanella, A. Piccioni, J. Kopula Kesavan, F. Boscherini, L. Pasquini, *Photochem. Photobiol. Sci.* **2019**, *18*, 2150.
- [23] M. J. Gira, K. P. Tkacz, J. R. Hampton, *Nano Converg.* **2016**, *3*, 6.
- [24] P. Connor, J. Schuch, B. Kaiser, W. Jaegermann, *Z. Phys. Chemie* **2020**, *234*, 979.
- [25] G. L. Chiarello, M. Bernareggi, M. Pedroni, M. Magni, S. M. Pietralunga, A. Tagliaferri, E. Vassallo, E. Selli, *J. Mater. Chem. A* **2017**, *5*, 12977.
- [26] S. Darmawi, S. Burkhardt, T. Leichtweiss, D. A. Weber, S. Wenzel, J. Janek, M. T. Elm, P. J. Klar, *Phys. Chem. Chem. Phys.* **2015**, *17*, 15903.
- [27] I. Rodríguez-Gutiérrez, E. Djatoubai, J. Su, A. Vega-Poot, G. Rodríguez-Gattorno, F. L. Souza, G. Oskam, *Sol. Energy Mater. Sol. Cells* **2020**, *208*, 110378.
- [28] C. Zachäus, Z. Zachäus, F. F. Abdi, L. M. Peter, R. Van De Krol, *Chem. Sci.* **2017**, *8*, 3712.
- [29] B. Moss, F. S. Hegner, S. Corby, S. Selim, L. Francàs, N. López, S. Giménez, J.-R. Galán-Mascarós, J. R. Durrant, *ACS Energy Lett.* **2019**, *4*, 337.
- [30] L. Meda, G. Tozzola, A. Tacca, G. Marra, S. Caramori, V. Cristino, C. Alberto Bignozzi, *Sol. Energy Mater. Sol. Cells* **2010**, *94*, 788.
- [31] J. A. Seabold, K.-S. Choi, *J. Am. Chem. Soc.* **2012**, *134*, 2186.